Biointerface Research in Applied Chemistry
Open-Access Journal (ISSN: 2069-5837)

Article
Volume 13, Issue 1, 2023, 8
https://doi.org/10.33263/BRIAC131.008

Structural and Electrochemical Properties of $NiFe_{2-x}Cu_xO_4$ Spinel for Oxygen Evolution Reaction

Derradji Sahnoune [1], Sofiane Makhloufi [1], Mahmoud Omari [1,*]

[1] Laboratory of Molecular Chemistry and Environment, University of Biskra, 07000 Algeria
* Correspondence: m2omari@yahoo.fr;

Scopus Author ID AAY-6605-2021
Received: 8.10.2021; Accepted: 15.11.2021; Published: 7.01.2022

Abstract: Developing new material oxides catalysts for the oxygen evolution reaction in alkaline media is important to enhance the efficiency of the water-splitting process. For this purpose, the effect of copper doping on the structural, morphological, and catalytic properties of $NiFe_2CuO_4$ oxides for the oxygen evolution reaction has been investigated. X-ray diffraction analysis of samples calcined at 1000 °C shows that the pure spinel structure was obtained in the range $0 \leq x \leq 0.4$. The FTIR spectra confirm the presence of the metal-oxygen bond of M-O in the tetrahedral and octahedral sites of the spinel structure. Scanning electron microscopy (SEM) shows that the calcined powders have a compact and dense surface and pronounced agglomeration. The OER results indicate that the $NiFe_2O_4$ electrode exhibits a higher performance with the current density of 26 $mA.cm^{-2}$ at 0.55 V and a small Tafel plot of 68 $mV.dec^{-1}$. Further investigations also accounted for the degradation of electrocatalytic activity with increasing copper content.

Keywords: Cu doped $NiFe_2O_4$; spinel ; sol-gel method; OER; electrocatalytic activity.

1. Introduction

Spinel structures are interesting subjects for practical applications and have been investigated in material science due to their physicochemical properties [1]. Nano-sized spinel ferrite gains a considerable interest for their application in various industrial processes for the fundamental understanding of their very different properties when the particle size approaches the atomic scale level [2–7].

$NiFe_2O_4$ is one of the most important spinel oxides due to its various applications in hyperthermia, catalysis [8-10], photodegradation of pollutants [11], and magnetic properties [12].

Many studies have been carried out to improve the catalytic properties of this material by metal ions modification. The substitution of nickel by metals has been mostly investigated. Among these materials, NiCoZn, NiW, and NiMo alloys have been used as electrocatalysts for the hydrogen evolution reaction (HER) in an alkaline media [13].

The biggest use of Ni with Fe in spinel is that iron has a great role in preventing the nickel electrode [14]. This compound exhibits catalytic properties for hydrogen evolution reaction [15], photocatalytic hydrogen evolution [16]. On the other hand, many works have been carried out to replace nobles' metals owing to their high cost and unavailability [17].

$NiFe_2O_4$ is a material with many desirable properties, such as high thermal conductivity, good mechanical resistance, chemical stability, and excellent electrochemical

properties [18]. Rao *et al*. [19] have reported that the increase of cobalt content improves the electronic conductivity of $NiFe_{2-x}Co_xO_4$ and the power density is maximum at 650 °C with NFCO-0.5 cathode. Zhao *et al*. [20] have demonstrated the potential applications of the Ag-doped $NiFe_2O_4$ for the catalyzed ozonation process of biologically recalcitrant wastewater. The catalytic and magnetic properties of $NiFe_2O_4$ and $Ni_{0.3}Zn_{0.7}Fe_2O_4$ during biodiesel production were reported [21]. It has been shown that a biodiesel yield of 94% was obtained with $Ni_{0.3}Zn_{0.7}Fe_2O_4$ and 49% with $NiFe_2O_4$.

Sulfur-incorporated $NiFe_2O_4$ nanosheets on nickel foam (S-$NiFe_2O_4$/NF) have been prepared by a confined growth strategy using thiourea and its catalytic properties were characterized for water splitting. It has been shown that this material exhibits remarkable catalytic activity, favorable kinetics, high Faradaic efficiency, and good stability towards both the oxygen and hydrogen evolution reactions [22].

The catalytic activity of zinc-doped $NiFe_2O_4$ synthesized by the co-precipitation method to degrade organic Methylene blue (MB) dye has been investigated. This study shows that the photocatalytic activity of $Ni_{1-x}Zn_xFe_2O_4$ using methylene blue is significant in a short period, and the recyclability tests show that these catalysts could be reused during 5 cycles without any important loss [23]. Later, Zhang *et al*. [24] have prepared mesoporous $NiFe_2O_4$/Nitrogen-doped carbon nanocomposite as anodes for lithium-ion batteries. The electrochemical data reveal that this material delivers a capacity as high as 760 $mAh \cdot g^{-1}$ at 0.2 °C after 50 cycles, and show good rate performance by remaining a capacity of 600 $mAh \cdot g^{-1}$ even at 1 °C. Thereafter, Zhang *et al*. [25] have studied the catalytic activity of $NiFe_2O_4$ by substituting nickel by cobalt into the spinel structure. It has been shown that Co's incorporation changes the rate-determining step and promotes the OER activity owing to the Ni-Co interaction-induced change in electronic properties.

Copper was previously used as a dopant into oxides to enhance their catalytic performances [26–30]. The effect of partially replacing iron with copper on the electrocatalytic activity of $NiFe_2O_4$ oxide for the oxygen evolution reaction has not been explored yet.

The purpose of our present work is to study the substitution effect of iron by copper on structural, morphological, and electrochemical properties of spinel ferrite $NiFe_{2-X}Cu_XO_4$ oxides ($0 \leq x \leq 0.5$) synthesized via the sol-gel method.

2. Materials and Methods

2.1. Synthesis.

$NiFe_{2-x}Cu_xO_4$ oxides with ($0 \leq x \leq 0.5$) were synthesized using the sol-gel method and citric acid as a complexing agent. The precursor salts $Ni(NO_3)_2 \cdot 6H_2O$ (BIOCHEM), $Fe(NO_3)_3 \cdot 9H_2O$ (BIOCHEM), and $Cu(NO_3)_2 \cdot 6H_2O$ (BIOCHEM) were first dissolved in propanol and added to a solution of citric acid (BIOCHEM). After that, the homogeneous solution was then heated at 80–100 °C for 4h. The obtained gel is heated for 24 h at 110 °C to remove the propanol. Then, the precursor is milled and calcined in air for 6 h at different calcination temperatures: 600-1000 °C with a heating rate of 5 $°C.min^{-1}$. We have designated calcined samples as follows NF (x = 0), NFC10 (x = 0.1), NFC20 (x = 0.2), NFC30 (x = 0.3), NFC40 (x = 0.4) and NFC 50 (x = 0.5).

2.2. Characterization techniques

The thermal analysis of the NFC10 powder was studied in the air using a SETARAM LABSYS Evo at a heating rate of 10 °C/min in air. The Fourier transform infrared measurements were made using FT-IR SHIMADZU 8400S spectrometer. X-ray diffraction (XRD) analysis was carried out with a D8 ADVANCE-BRUCKER using a Cu Ka radiation (kKa = 1.54056 Å) in the range 10–90° to identify the crystalline phases present in the calcined powders by comparison with, Joint Committee on Powder Diffraction Standards (JCPDS).

The particle morphology of the powder was analyzed using a Scanning electron microscopy (SEM) JEOL scanning electron microscope (Model JSM6390LV). The electrochemical measurements for the oxygen evolution reaction were performed using a PARSTAT 4000 potentiostat/galvanostat in a three-compartment cell. The working electrodes ($1cm^2$) were prepared by painting the nickel substrate with an oxide suspension. Pt plate and Ag/AgCl are used as the counter electrode and the reference electrode in 1M KOH, respectively. All potentials in the text have been referred to the Ag/AgCl electrode.

3. Results and Discussion

3.1. Thermal study.

The thermal behavior of the NFC10 powder precursor was investigated using thermogravimetric and differential thermal analysis (TG/DTA) in the temperature range 25-1000 °C. As shown in Figure1, the TG curve can be divided into four stages of weight loss : (1) 25- 180 °C, (2) 180- 370 °C, (3) 370- 630 °C and 630- 1000°C with corresponding weight losses of (-5.14%), (-56.57%), (-16.12) and (-2%) respectively. Firstly, a weight loss is accompanied by a sharp endothermic peak at about 138 °C in DTA curve. It can be attributed to removing moisture and the decomposition of the unreacted nitrate salts [31,32]. In the second range, two exothermic peaks are observed at around 215 °C and 330 °C, which can be assigned to the decomposition of citrates and nitrates [3,33].

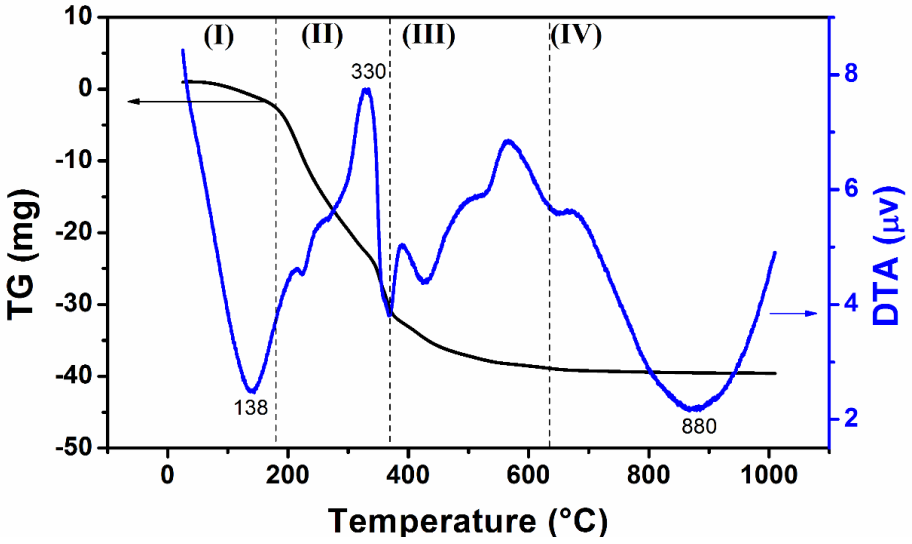

Figure 1. TG-DTA of NFC10 precursor calcined in air at 10 °C min^{-1}.

The highest reduction in weight was determined in stage (III), corresponding to the observation of two exothermic peaks centered at 390 and 565 °C is attributed to the joint decomposition of carbonate carboxylate-type complexes remaining in the sample [4]. In the

last range, a large endothermic peak was observed at 880 °C, which is possibly ascribed to the formation of the NFC10 spinel phase.

3.2. X-ray diffraction analysis.

X-ray diffraction (XRD) patterns were used to analyze the phase structure of samples. Figure 2 presents XRD patterns of the NFC10 powders at different sintering temperatures at 600, 700, 800, 900, and 1000 °C for 6 h. The diffraction peaks were identified at 30.2°, 35.6°, 43.3°, 53.8, 57.4° and 62.8° corresponding to the crystal planes of (220), (311), (400), (422), (511), and (440) for the cubic $NiFe_2O_4$ phase [6]. However, a small number of impurity peaks were indexed from the secondary phase Fe_2O_3 (JCPDS N°. 01-073-2234) and NiO (JCPDS N°. 01-089-5881) at T ≤ 900 °C. Furthermore, with the sintering temperature increased to 1000 °C, the impurity peaks of Fe_2O_3 and NiO disappeared, and only pure NFC10 cubic phase was detected. The crystallization temperature of NFC10 in TG-DTA is slightly different than observed in XRD, probably due to the difference in the heating program.

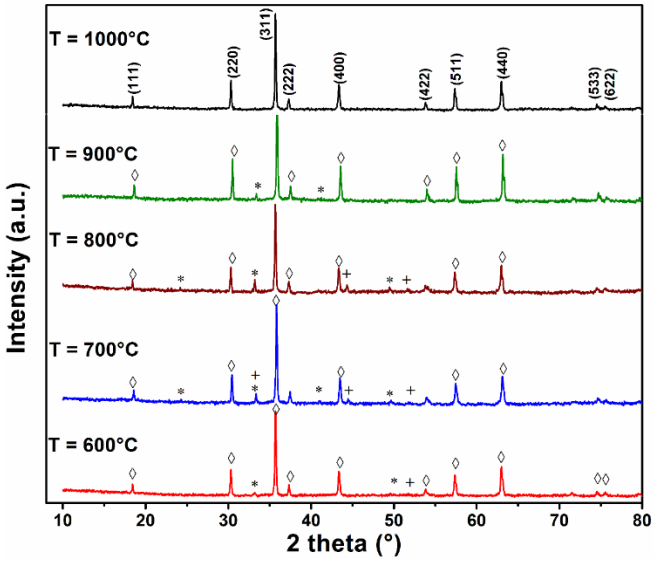

Figure 2. XRD patterns of the NFC10 composition: (*) Fe_2O_3; (+) NiO; (◊) cubic spinel phase.

The phase and purity of the as-synthesized $NiFe_{2-x}Cu_xO_4$ ($0 \leq x \leq 0.5$) calcined at 1000 °C were examined by X-ray diffraction (XRD) pattern and are shown in Figure 3. The observed sharp peaks indicate a good and high crystallinity of the prepared powders. The pure spinel phase with cubic structure, Fd3m space group (JCPDS N°. 00-044-1485), was formed, and no other diffraction peaks can be detected when x is ≤ 0.4, suggesting a high solubility of copper in NF system. However, at higher dopant content x = 0.5, a new secondary phase appeared from the impurity of CuO (JCPDS N°. 01-080-0076) with low intensity, which reveals that the solubility of Cu ions into the $NiFe_2O_4$ lattice is reached in the composition range $0.0 \leq x \leq 0.4$.

The lattice parameters of the spinel $NiFe_{2-x}Cu_xO_4$ were calculated using XRD patterns. The values of cell parameters (Å) and volume ($Å^3$) are summarized in Table1. The positions of the characteristic peaks shift to lower angles with an increase in the copper content (x), indicating a lattice size expansion at higher copper content since the ionic radius of Fe^{3+} (0.64 Å) is smaller than that of Cu^{2+} (0.73 Å). A similar tendency has already been found for Co-doped $LaNiO_3$ samples [34].

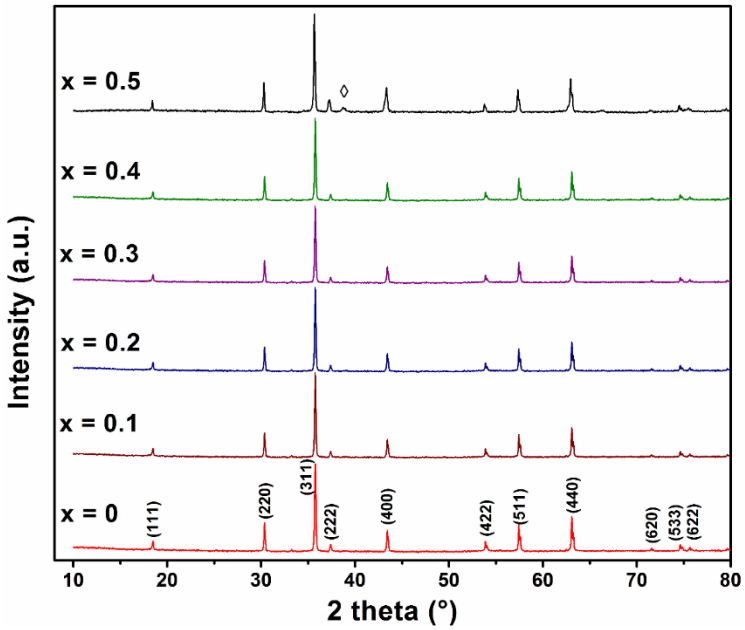

Figure 3. X-ray diffraction patterns of synthesized $NiFe_{2-x}Cu_xO_4$ ($0 \leq x \leq 0.5$) after calcination at 1000 °C, (◊) : CuO.

Table 1. Values of unit cell parameters for $NiFe_{2-x}Cu_xO_4$.

Composition	a =b=c (Å)	V (Å^3)
NF	8.345	581.14
NFC10	8.340	580.11
NFC20	8.338	579.75
NFC30	8.335	579.39
NFC40	8.333	579.14
NFC50	8.332	579.02

3.3. FT-IR analysis.

The FTIR spectra of the prepared electrocatalysts $NiFe_{2-x}Cu_xO_4$ ($0 \leq x \leq 0.5$) calcined at 1000 °C for 6h are shown in Figure 4.

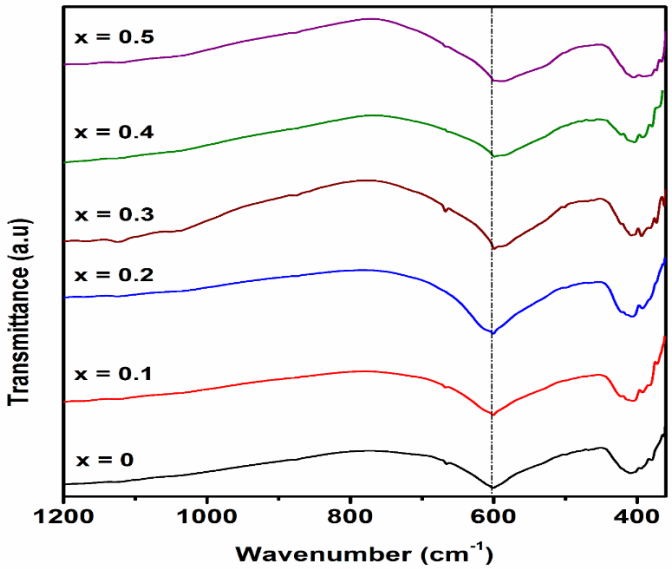

Figure 4. Infrared spectra of $NiFe_{2-x}Cu_xO_4$ ($0 \leq x \leq 0.5$) samples calcined at 1000 °C.

All these spectra are similar in shape. Each spectrum shows strong and well-defined absorption bands, typical of spinel oxides [35]. The strong peaks observed at 602 and 408 cm^{-1} are ascribed to the M-O bonds at the tetrahedral and octahedral sites of the spinel structure

[35]. This result is also in agreement with previous work [36], which indicates that the low-frequency bands are assigned to an octahedral group ($450 \leq \upsilon \leq 400$ cm^{-1}) and the high-frequency bands to the tetrahedral group ($630 \leq \upsilon \leq 555$ cm^{-1} regions). These bands shift toward shorter wavenumbers by increasing iron substitution by copper. This is probably due to the two different crystallographic positions of B cations in the cubic-distorted spinel lattice. A similar trend has been found previously [37].

3.4. Structural and morphological characterization.

The average crystallite size (D) (Figure 5) was estimated using the Debye-Scherrer relationship, considering the peak (311) of the spinel-type $NiFe_{2-x}Cu_xO_4$ oxides. The obtained crystallite sizes are in the range 30.2–66.3 nm, indicating that the mixed oxides powders are composed of nanometric particles.

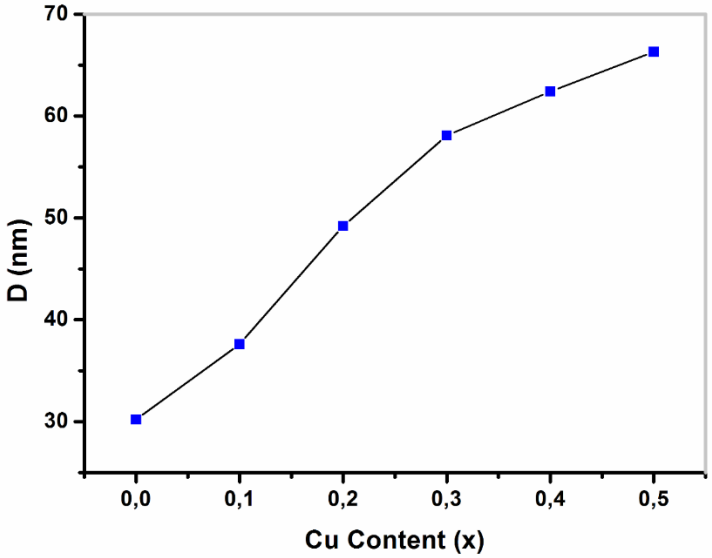

Figure 5. Crystallite size of $NiFe_{2-x}Cu_xO_4$ ($0 \leq x \leq 0.5$) powders.

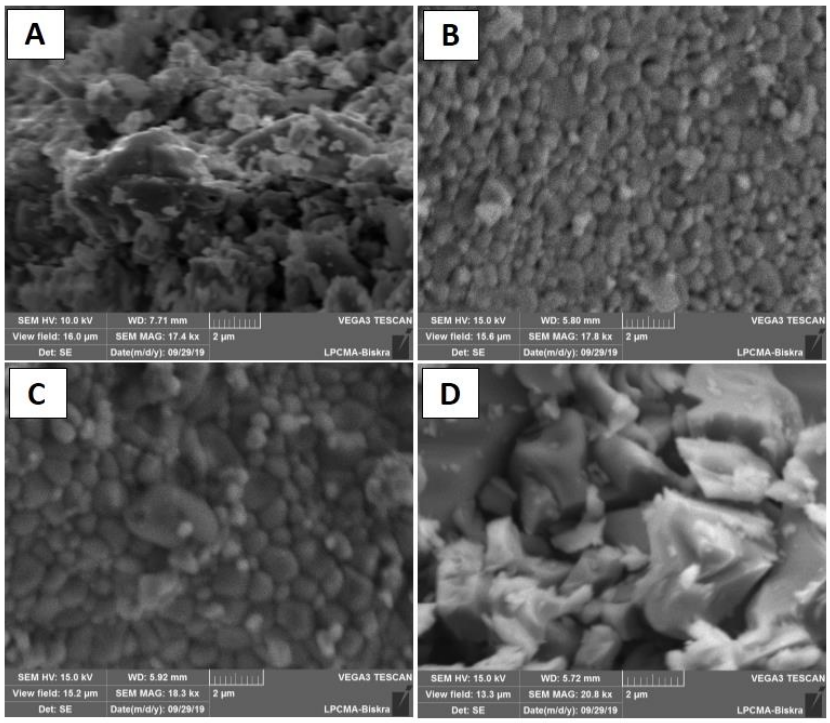

Figure 6. SEM micrographs of $NiFe_{2-x}Cu_xO_4$, A: x = 0; B: x = 0.1; C: x = 0.2; D: x = 0.3 calcined at 1000 °C.

The crystallite size increases with increasing cobalt content, probably due to the incorporation of Cu^{2+} into the $NiFe_2O_4$ lattice, leading to crystallite growth. Moreover, a similar result was also found previously for Zn-substituted $MnCo_2O_4$ samples synthesized by simple hydrothermal technique [38]. The morphologies of $NiFe_{2-x}Cu_xO_4$ ($0 \leq x \leq 0.3$) samples studied by SEM are shown in (Figure 6). The powders are constituted of macro-agglomerated particles with different sizes and forms (particle-particle interactions), which is possibly due to the nature of the solvent used in the preparation of the precursor. A non-uniform distribution with some clustered particles is observed. These powders seem to have a nonporous surface. Moreover, the surface morphology indicates a dense microstructure.

3.5. Electrochemical properties.

The electrocatalytic activity of the as-prepared $NiFe_{2-x}Cu_xO_4$ catalysts for the oxygen evolution reaction (OER) in alkaline media (1M KOH) was investigated by the linear sweep voltammetry (LSV) in an interval of 0 – 0.65 V using a sweep rate of 50 $mV.s^{-1}$ (Figure 7). We observe in general that these electrodes have qualitatively similar behavior. The coated electrode films showed good cohesion through polarization. Each voltammogram presents one anodic peak (430 mV ≤ Epa ≤ 500 mV) attributed to the Ni(II)/Ni(III) redox couple [39,40].

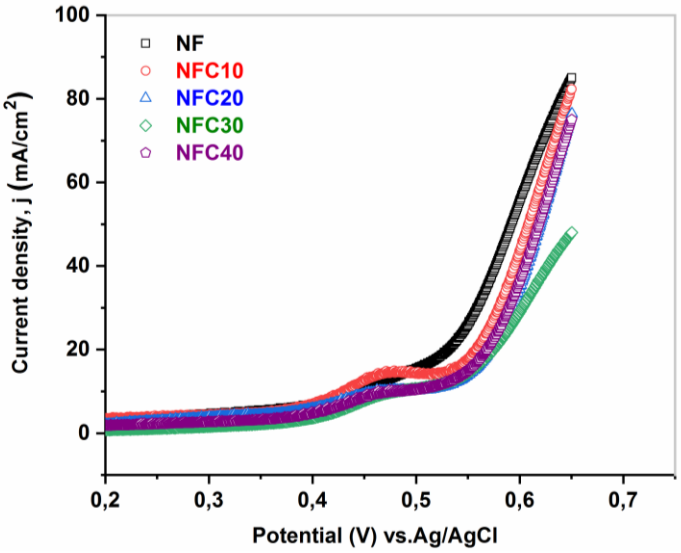

Figure 7. Linear sweep voltammograms of $NiFe_{2-x}Cu_xO_4$ ($0 \leq x \leq 0.4$) calcined at 1000 °C.

A slight shift in the position of redox peaks at the higher potential region is detected. It may be ascribed to the synergistic interaction between Ni metal (substrate) and $NiFe_{2-x}Cu_xO_4$ catalysts [41]. Thus, pure Ni used as the support in the present study may produce an oxidation-reduction (Ni^{2+}/Ni^{3+}) reaction during the anodic region due to the electrolyte contact through pores, cracks, and so on [5,42]. The anodic current obtained at a potential greater than E > 500 mV is due to the oxygen evolution reaction.

The current density increases according to the following order: NFC40 ≈ NFC30 ≈ NFC20 < NFC10 < NF. The NF electrode shows a higher current density (~ 26 $mA.cm^{-2}$) at 0.55 V compared to the other samples. These results clearly indicate that better electroactivity toward the OER can be achieved with the NF electrode.

The increase of copper content reduces the electroactivity of these electrodes. The same results were also found in [43]. It has been reported that $LaMnO_3$ exhibits better performance for the OER compared to $LaMn_{0.5}Cu_{0.5}O_3$. This finding was explained by the e_g orbital filling

of B-sites in $LaMnO_3$ is close to unity while it is lower (~ 0.3) for the doped sample. The e_g orbital of the transition metal B filling approached to unity facilitates the rate-determining step, strongly enhancing the OER activity. Guo *et al*. [44] have indicated that the electrons in the e_g orbitals can affect the oxygen-containing intermediate bonds, in particular for OH*, during OER, which optimizes its performance. The better performance of the undoped electrode for the OER is probably because only Fe-site doping deviates from the optimal e_g filling [45].

On the other hand, the same trend of the OER performance was also obtained when nickel is substituted by cobalt in $NiFe_2O_4$. Indeed, this result was explained by the possible negative effect of the presence of more oxygen vacancies in the doped sample compared to the parent oxide [46].

The activity of NF has been compared with other OER electrocatalysts and shown in Figure 8. The NF electrode exhibits the better performance (~ 26 $mA.cm^{-2}$) at 0.55 V vs Ag/AgCl compared to other materials CoO_4 (~ 1 $mA.cm^{-2}$) , Pt/C (~ 1 $mA.cm^{-2}$), $NiCo_2O_4$ (~ 2 $mA.cm^{-2}$) [47], RuO_2 (~ 20 $mA.cm^{-2}$) [44], IrO_2 (~ 20 $mA.cm^{-2}$), Mn_2CoO_4 (~ 5 $mA.cm^{-2}$), dual-phase $MnCo_2O_4$ (~ 10 $mA.cm^{-2}$) [48], $CoFe_2O_4$ (~ 2.5 $mA.cm^{-2}$) [49], $CoMoO_4$ (~ 1 $mA.cm^{-2}$), $CoMoO_{4-x}S_x$ (~ 3 $mA.cm^{-2}$), $Fe_{0.5}Co_{0.5}MoO_4$ (~ 4 $mA.cm^{-2}$) [50]. These values confirm the OER performance in NF electrocatalysts compared to that of previous reports.

The obtained Tafel plots were used to estimate the catalytic reaction kinetics of the catalysts (Figure 8). The obtained values at low potential are 68, 75, 81, 83 and 87 $mV.dec^{-1}$ for NF, NFC10, NFC20, NFC30 and NFC40 respectively. The Tafel slope of NF was 68 mV dec^{-1}, which was smaller than the doped samples, implying better reaction kinetics within a certain potential range. The electrodes NFC20, NFC30, and NFC40 show similar OER performance in Tafel slope and current density. This shows that adding more copper has no significant effect on OER performance for compositions $x \geq 0.2$, which is in good agreement with LSV results.

The general possible OER mechanism of these catalysts [51–53] is:

$$S + OH^- \rightarrow S\text{-}OH + e^-$$
$$S\text{-}OH + OH^- \rightarrow S\text{-}O + H_2O + e^-$$
$$S\text{-}O + OH^- \rightarrow S\text{-}OOH + e^-$$
$$S\text{-}OOH + OH^- \rightarrow S\text{-}OO + H_2O + e^-$$
$$S\text{-}OO \rightarrow S + O_2$$

where S is active sites, the second step is assumed as the rate-determining step.

This mechanism is only tentative, and others could be considered. The strength of interactions between the oxide surface and the oxygenated intermediates strongly influences the rate-determining step [54]. This indicates that the variation of the Tafel slope from 68 to 87 $mV.dec^{-1}$ is probably due to the increase of difficulty of the first step to occur.

Further, an EIS study was carried out to examine the charge transfer kinetics and the adsorption of intermediates at the electrode interface. Figure 9 shows the representative EIS of Nyquist plots measured in the frequency range of 100 kHz to 10 mHz at 550 mV. In the case of all the electrodes, two quasi-semicircles were observed in high and low-frequency regions, associated with metal oxide and OER properties of the catalysts. Semicircle observed at low-frequency regions is mainly due to adsorption/desorption of (H^+/OH^-) reactive intermediates by relaxation and diffusion of charge-associated surface intermediates, whereas at high frequency corresponds the response of charge transfer resistance [55].

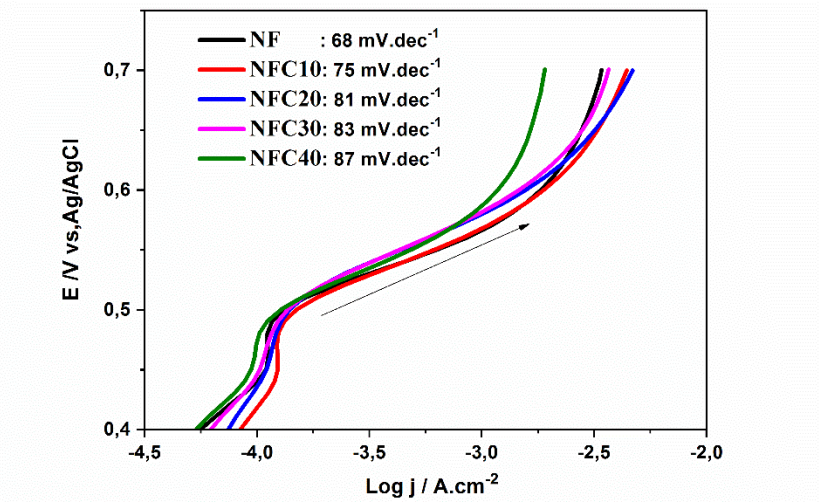

Figure 8. Tafel plots of $NiFe_{2-x}Cu_xO_4$ ($0 \leq x \leq 0.4$) calcined at 1000 °C.

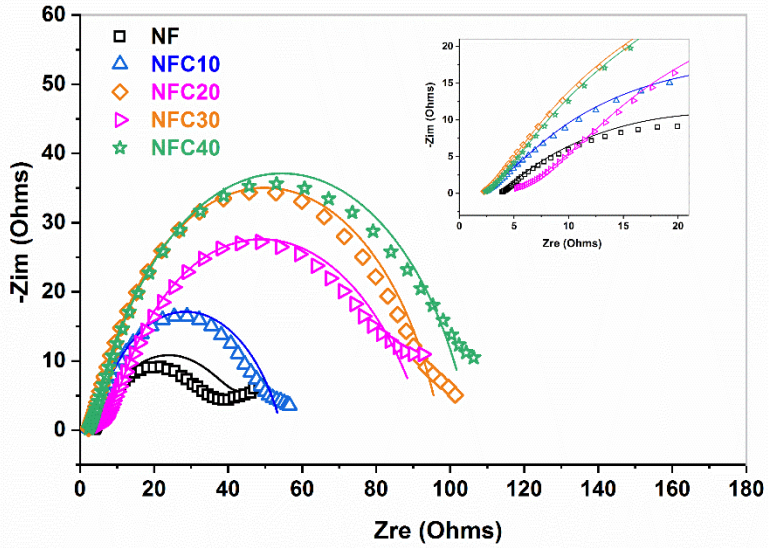

Figure 9. Nyquist diagrams of of $NiFe_{2-x}Cu_xO_4$ ($0 \leq x \leq 0.4$) electrodes at 0.55 V.

The best fit of experimental data with equivalent circuit model was found with R_S (Q_{dl} (R_{ct} W)) for the undoped sample and R_S (C_{ad} R_{ad} (Q_{dl} R_{ct})(Q_0 R_0)) for the other samples. In the two EC models, R_S, Q_{dl}, R_{ct}, W denote the solution resistance, The double-layer capacitance, the charge transfer resistance, and Warburg impedance, respectively.

($Q_{ads}R_{ads}$) is the impedance of O-intermediate (OH_{ads}) adsorption, which results in a relaxation process of these species [56], and (Q_0 R_0) is the impedance of metal oxide.

Table 2. Values of the circuit parameters of $NiFe_{2-x}Cu_xO_4$ ($0 \leq x \leq 0.4$) electrodes at 0.55 V.

Electrode	R_s (Ω)	$Q_{dl} \times 10^{-3}$ ($\Omega^{-1}S^n$)	R_{ct} (Ω)	$W \times 10^{-1}$ (Ω^{-1})	----	----	----
NF	3.94 ± 0.02	2.81 ± 0.10	38.60 ± 0.04	2.76 ± 0.50	----	----	----
	R_s (Ω)	$C_O \times 10^{-5}$ (F)	R_O (Ω)	$Q_{dl} \times 10^{-5}$ ($\Omega^{-1}S^n$)	R_{ct} (Ω)	$Q_{ads} \times 10^{-4}$ ($\Omega^{-1}S^n$)	R_{ads}(Ω)
NFC10	2.48 ± 0.02	5.21 ± 0.16	1.25 ± 0.21	143.00 ± 0.16	52.15 ± 0.01	5.29 ± 0.23	55.91 ± 0.14
NFC20	2.27 ± 0.09	5.77 ± 0.09	50.79 ± 0.81	6.12 ± 0.20	95.17 ± 0.01	7.73 ± 0.02	1.40 ± 0.12
NFC30	5.05 ± 0.02	2.14 ± 0.15	49.70 ± 0.51	9.07 ± 0.20	88.11 ± 0.01	15.70 ± 0.01	1.76 ± 0.08
NFC40	2.41 ± 0.01	6.29 ± 0.13	1.24 ± 0.50	71.10 ± 0.25	103.00 ± 0.01	5.69 ± 0.20	10.35 ± 0.10

The parameters estimated from the best-fitted circuit, which explains the behavior of the electrodes, have been tabulated in Table 2.

The electrolyte resistance oscillates between 2.27 and 5.046 Ω, which may be related to some systematic increase in the wiring resistance used in the OER measurements. This finding agrees with previous work indicating the decrease of the conductivity with increasing copper content [60]. The C_{dl}, the pseudo-capacitance, shows values of the order of 10^{-5}–10^{-3} F cm^{-2}, which are slightly higher than those reported previously [57,58]. The electrochemically active surface area is proportional to the double-layer capacitance [59], indicating that the C_{dl} value characterizes the OER activity. The highest value of the C_{dl} ($2.81.10^{-3}$ $F.cm^{2}$) for the NF electrode is consistent with its high electroactivity. This is probably due to its high active site density than the other electrodes, which improves its catalytic properties.

4. Conclusions

In summary, we have successfully prepared the Cu-doped $NiFe_2O_4$ ($0 \leq x \leq 0.5$) powders using the citrate sol-gel method, employing nitrate salts of nickel, iron, and copper as cations precursors, citric acid as a chelating agent. TG-DTA curves show the thermochemical behavior of the precursors' samples with respect to temperature. According to XRD patterns, $NiFe_{2-x}Cu_xO_4$ oxides exhibit a pure cubic structure with Fd3m space group at 1000 °C in the range ($0.0 \leq x \leq 0.4$). One detectable secondary phase from the impurity of CuO is observed for $x = 0.5$, indicating that solubility is reached for $x < 0.5$. FTIR spectra show two strong peaks ascribe to the M-O bonds at the tetrahedral and octahedral sites of the spinel structure. The morphology of products examined by SEM shows compounds have a compact and dense surface, with very well pronounced agglomeration. The activity for the OER increases according to the following order: NFC40 ≈ NFC30 ≈ NFC20 < NFC10 < NF. As a result of the electrocatalytic activity, the NF electrode exhibits outstanding OER performance with higher current density (~ 26 $mA.cm^{-2}$) at 0.55 V and a small Tafel slope (68 $mV.dec^{-1}$). The copper substitution has considerably influenced the OER in alkaline media. The decrease of catalytic activity can be ascribed to the surface and electronic properties that act negatively on these materials' performance.

Funding

This research received no external funding.

Acknowledgments

This work was supported by the directorate general of scientific research and technological development-DGRSDT of Algeria.

Conflicts of Interest

The authors declare no conflict of interest.

References

1. Groven, L.; Pfeil, T.; Pourpoint, T. Solution combustion synthesized cobalt oxide catalyst precursor for $NaBH_4$ hydrolysis. *Int. J. Hydrogen Energy* **2013**, *38*, 6377–6380, https://doi.org/10.1016/j.ijhydene.2013.03.060.

2. Talluri, B.; Aparna, M.; Sreenivasulu, N.; Bhattacharya, S.; Thomas, T. High entropy spinel metal oxide $(CoCrFeMnNi)_3O_4$ nanoparticles as a high-performance supercapacitor electrode material. *J. Energy Storage* **2021**, *42*, 103004, https://doi.org/10.1016/j.est.2021.103004.
3. Ren, F.; Zhu, W.; Zhao, J.; Liu, H.; Zhang, X.; Zhang, H.; Zhu, H.; Peng, Y.; Wang, B. Nitrogen-doped graphene oxide aerogel anchored with spinel $CoFe_2O_4$ nanoparticles for rapid degradation of tetracycline. *Sep. Purif. Technol.* **2020**, *241*, 116690, https://doi.org/10.1016/j.seppur.2020.116690.
4. Huang, M.; Lv, S.; Zhou, C. Thermal decomposition kinetics of glycine in nitrogen atmosphere. *Thermochim. Acta* **2013**, *552*, 60–64, https://doi.org/10.1016/j.tca.2012.11.006.
5. Rahman, A.; Zulfiqar, S.; Haq, A.U.; Alsafari, I.A.; Qazi, U.Y.; Warsi, M.F.; Shahid, M. Cd-Gd-doped nickel spinel ferrite nanoparticles and their nanocomposites with reduced graphene oxide for catalysis and antibacterial activity studies. *Ceram. Int.* **2020**, *47*, 9513–9521, https://doi.org/10.1016/j.ceramint.2020.12.085.
6. Kooti, M.; Sedeh, A.N. Synthesis and Characterization of $NiFe_2O_4$ Magnetic Nanoparticles by Combustion Method. *J. Mater. Sci. Technol.* **2013**, *29*, 34–38, https://doi.org/10.1016/j.jmst.2012.11.016.
7. Sivakumar, P.; Ramesh, R.; Ramanand, A.; Ponnusamy, S.; Muthamizhchelvan, C. Synthesis and characterization of $NiFe_2O_4$ nanoparticles and nanorods. *J. Alloy. Compd.* **2013**, *563*, 6–11, https://doi.org/10.1016/j.jallcom.2013.02.077.
8. Li, N.; Sun, L.; Li, Q.; Xia, T.; Huo, L.; Zhao, H. Electrode properties of CuBi2O4 spinel oxide as a new and potential cathode material for solid oxide fuel cells. *J. Power Sources* **2021**, *511*, 230447, https://doi.org/10.1016/j.jpowsour.2021.230447.
9. Ramakrishnan, P.; BLee, K.; ISohn, J. Ternary metal-based inverse spinel oxide $NiCrFeO_4$ nanoparticles as a highly efficient oxygen evolution catalyst. *Appl. Surf.Sci* **2021**, *566*, 150653, https://doi.org/10.1016/j.apsusc.2021.150653
10. Liu, W.; Han, J.; Yamada, I.; Yagi, S. Effects of zinc ions at tetrahedral sites in spinel oxides on catalytic activity for oxygen evolution reaction. *J. Catal.* **2021**, *394*, 50–57, https://doi.org/10.1016/j.jcat.2020.12.014.
11. Kirankumar, V.; Sumathi, S. A review on photodegradation of organic pollutants using spinel oxide. *Mater. Today Chem.* **2020**, *18*, https://doi.org/10.1016/j.mtchem.2020.100355.
12. Borah, R.; Ravi, S. Effect of cation distributions on structural and magnetic properties of $Ni_{1-x}Co_xFe_2O_4$ spinel ferrites. *J. Magn. Magn. Mater.* **2021**, *538*, 168276, https://doi.org/10.1016/j.jmmm.2021.168276.
13. Wang, M.; Wang, Z.; Guo, Z.; Li, Z. The enhanced electrocatalytic activity and stability of NiW films electrodeposited under super gravity field for hydrogen evolution reaction. *Int. J. Hydrogen Energy* **2011**, *36*, 3305–3312, https://doi.org/10.1016/j.ijhydene.2010.12.116.
14. Mauer, A.E.; Kirk, D.W.; Thorpe, S.J. The role of iron in the prevention of nickel electrode deactivation in alkaline electrolysis. *Electrochimica Acta* **2007**, *52*, 3505–3509, https://doi.org/10.1016/j.electacta.2006.10.037.
15. Navarro-Flores, E.; Chong, Z.; Omanovic, S. Characterization of Ni, NiMo, NiW and NiFe electroactive coatings as electrocatalysts for hydrogen evolution in an acidic medium. *J. Mol. Catal. A: Chem.* **2005**, *226*, 179–197, https://doi.org/10.1016/j.molcata.2004.10.029.
16. Rekhila, G.; Bessekhouad, Y.; Trari, M. Visible light hydrogen production on the novel ferrite $NiFe_2O_4$. *Int. J. Hydrogen Energy* **2013**, *38*, 6335–6343, https://doi.org/10.1016/j.ijhydene.2013.03.087.
17. Song, W.; Poyraz, A.S.; Meng, Y.; Ren, Z.; Chen, S.-Y.; Suib, S.L. Mesoporous Co_3O_4 with Controlled Porosity: Inverse Micelle Synthesis and High-Performance Catalytic CO Oxidation at −60 °C. *Chem. Mater.* **2014**, *26*, 4629–4639, https://doi.org/10.1021/cm502106v.
18. Landon, J.; Demeter, E.; Inoğlu, N.; Keturakis, C.; Wachs, I.E.; Vasić, R.; Frenkel, A.I.; Kitchin, J.R. Spectroscopic Characterization of Mixed Fe–Ni Oxide Electrocatalysts for the Oxygen Evolution Reaction in Alkaline Electrolytes. *ACS Catal.* **2012**, *2*, 1793–1801, https://doi.org/10.1021/cs3002644.
19. Rao, Y.; Wang, Z.; Chen, L.; Wu, R.; Peng, R.; Lu, Y. Structural, electrical, and electrochemical properties of cobalt-doped $NiFe_2O_4$ as a potential cathode material for solid oxide fuel cells. *Int. J. Hydrogen Energy* **2013**, *38*, 14329–14336, https://doi.org/10.1016/j.ijhydene.2013.08.097.
20. Zhao, J.; Cao, J.; Zhao, Y.; Zhang, T.; Zheng, D.; Li, C. Catalytic ozonation treatment of papermaking wastewater by Ag-doped $NiFe_2O_4$: Performance and mechanism. *J. Environ. Sci.* **2020**, *97*, 75–84, https://doi.org/10.1016/j.jes.2020.04.014.
21. Mapossa, A.B.; Dantas, J.; Silva, M.R.; Kiminami, R.H.; Costa, A.C.F.; Daramola, M. Catalytic performance of $NiFe_2O_4$ and $Ni_{0.3}Zn_{0.7}Fe_2O_4$ magnetic nanoparticles during biodiesel production. *Arab. J. Chem.* **2019**, *13*, 4462–4476, https://doi.org/10.1016/j.arabjc.2019.09.003.
22. Liu, J.; Zhu, D.; Ling, T.; Vasileff, A.; Qiao, S.Z. S- $NiFe_2O_4$ ultra-small nanoparticle built nanosheets for efficient water splitting in alkaline and neutral pH. *Nano Energy* **2017**, *40*, 264–273, https://doi.org/10.1016/j.nanoen.2017.08.031.
23. Vinosha, P.; Xavier, B.; Krishnan, S.; Das, S. Investigation on zinc substituted highly porous improved catalytic activity of $NiFe_2O_4$ nanocrystal by co-precipitation method. *Mater. Res. Bull.* **2018**, *101*, 190–198, https://doi.org/10.1016/j.materresbull.2018.01.026.

24. Zhang, J.; Chen, Z.H. Preparation and Electrochemical Properties of Mesoporous $NiFe_2O_4$/N-Doped Carbon Nanocomposite as an Anode for Lithium Ion Battery. *Front. Mater.* **2020**, *7* , 1-8, https://doi.org/10.3389/fmats.2020.00178
25. Zhang, Z.; Yan, X.; Liu, J.; Liu, B.; Gu, Z.-G. Tailoring the catalytic activity of nickel sites in $NiFe_2O_4$ by cobalt substitution for highly enhanced oxygen evolution reaction. *Sustain. Energy Fuels* **2021**, *5*, 2668–2677, https://doi.org/10.1039/d1se00318f.
26. Adaika, K.; Omari, M. Synthesis and physicochemical characterization of $LaCr_{1-x}Cu_xO_3$. *J. Sol-Gel Sci. Technol.* **2015**, *75*, 298–304, https://doi.org/10.1007/s10971-015-3699-z.
27. Zhang, R.; Villanueva, A.; Alamdari, H.; Kaliaguine, S. Reduction of NO by CO over nanoscale $LaCo_{1-x}Cu_xO_3$ and $LaMn_{1-x}Cu_xO_3$ perovskites. *J. Mol. Catal. A: Chem.* **2006**, *258*, 22–34, https://doi.org/10.1016/j.molcata.2006.05.008.
28. Zhu, H.; Chen, Y.; Wang, Z.; Liu, W.; Wang, L. Catalytic oxidation of CO over mesoporous copper-doped ceria catalysts via a facile CTAB-assisted synthesis. *RSC Adv.* **2018**, *8*, 14888–14897, https://doi.org/10.1039/c8ra02327a.
29. Niu, X.; Lei, Z. Copper doped manganese oxides to produce enhanced catalytic performance for CO oxidation. *J. Environ. Chem. Eng.* **2019**, *7*, 103055, https://doi.org/10.1016/j.jece.2019.103055.
30. Omari, E.; Omari, M. Cu-doped $GdFeO_3$ perovskites as electrocatalysts for the oxygen evolution reaction in alkaline media. *Int. J. Hydrogen Energy* **2019**, *44*, 28769–28779, https://doi.org/10.1016/j.ijhydene.2019.09.088.
31. Omari, E.; Omari, M.; Barkat, D. Oxygen evolution reaction over copper and zinc co-doped $LaFeO_3$ perovskite oxides. *Polyhedron* **2018**, *156*, 116–122, https://doi.org/10.1016/j.poly.2018.09.031.
32. Zhao, S.; Wang, Y.; Wang, L.; Jin, Y. Preparation, characterization and catalytic application of hierarchically porous $LaFeO_3$ from a pomelo peel template. *Inorg. Chem. Front.* **2017**, *4*, 994–1002, https://doi.org/10.1039/c6qi00600k.
33. Omari, E.; Makhloufi, S.; Omari, M. Preparation by Sol–Gel Method and Characterization of Co-doped $LaNiO_3$ Perovskite. *J. Inorg. Organomet. Polym. Mater.* **2017**, *27*, 1466–1472, https://doi.org/10.1007/s10904-017-0604-y.
34. Rebekah, A.; Kumar, E.A.; Viswanathan, C.; Ponpandian, N. Effect of cation substitution in $MnCo_2O_4$ spinel anchored over rGO for enhancing the electrocatalytic activity towards oxygen evolution reaction (OER). *Int. J. Hydrogen Energy* **2020**, *45*, 6391–6403, https://doi.org/10.1016/j.ijhydene.2019.12.164.
35. Waldron, R.D. Infrared Spectra of Ferrites. *Phys. Rev.* **1955**, *99*, 1727–1735, https://doi.org/10.1103/physrev.99.1727.
36. Makhloufi, S.; Omari, M. Structural, Electrical and Electrochemical Characterizations of Perovskite Ni-Doped $SrCoO_{3-\delta}$. *J. Inorg. Organomet. Polym. Mater.* **2015**, *26*, 32–40, https://doi.org/10.1007/s10904-015-0295-1.
37. Rebekah, A.; Anantharaj, S.; Viswanthan, C.; Ponpandian, N. Zn-substituted $MnCo_2O_4$ nanostructure anchored over rGO for boosting the electrocatalytic performance towards methanol oxidation and oxygen evolution reaction (OER). *Int. J. Hydrogen Energy* **2020**, *45*, 14713–14727, https://doi.org/10.1016/j.ijhydene.2020.03.231.
38. Singh, R.; Madhu; Awasthi, R.; Tiwari, S. Iron molybdates as electrocatalysts for O_2 evolution reaction in alkaline solutions. *Int. J. Hydrogen Energy* **2009**, *34*, 4693–4700, https://doi.org/10.1016/j.ijhydene.2009.04.006.
39. Egelund, S.; Caspersen, M.; Nikiforov, A.; Møller, P. Manufacturing of a $LaNiO_3$ composite electrode for oxygen evolution in commercial alkaline water electrolysis. *Int. J. Hydrogen Energy* **2016**, *41*, 10152–10160, https://doi.org/10.1016/j.ijhydene.2016.05.013.
40. Singh, R.; Madhu; Awasthi, R.; Sinha, A. Electrochemical characterization of a new binary oxide of Mo with Co for O_2 evolution in alkaline solution. *Electrochimica Acta* **2009**, *54*, 3020–3025, https://doi.org/10.1016/j.electacta.2008.12.012.
41. Raghuveer, V. Rare earth cuprates as electrocatalysts for methanol oxidation. *Solid State Ionics* **2001**, *140*, 263–274, https://doi.org/10.1016/s0167-2738(01)00816-5.
42. Suntivich, J.; May, K.J.; Gasteiger, H.A.; Goodenough, J.B.; Shao-Horn, Y. A Perovskite Oxide Optimized for Oxygen Evolution Catalysis from Molecular Orbital Principles. *Science* **2011**, *334*, 1383–1385, https://doi.org/10.1126/science.1212858.
43. Guo, Q.; Li, X.; Wei, H.; Liu, Y.; Li, L.; Yang, X.; Zhang, X.; Liu, H.; Lu, Z. Sr, Fe Co-doped Perovskite Oxides with High Performance for Oxygen Evolution Reaction. *Front. Chem.* **2019**, *7*, https://doi.org/10.3389/fchem.2019.00224.
44. Guo, Y.; Tong, Y.; Chen, P.; Xu, K.; Zhao, J.; Lin, Y.; Chu, W.; Peng, Z.; Wu, C.; Xie, Y. Engineering the Electronic State of a Perovskite Electrocatalyst for Synergistically Enhanced Oxygen Evolution Reaction. *Adv. Mater.* **2015**, *27*, 5989–5994, https://doi.org/10.1002/adma.201502024.
45. Pal, S.; Azad, U.P.; Singh, A.K.; Kumar, D.; Prakash, R. Studies on some spinel oxides based electrocatalysts for oxygen evolution and capacitive applications. *Electrochimica Acta* **2019**, *320*, 134584, https://doi.org/10.1016/j.electacta.2019.134584.

46. Béjar, J.; Alvarez-Contreras, L.; Ledesma-García, J.; Arjona, N.; Arriaga, L. Electrocatalytic evaluation of Co_3O_4 and $NiCo_2O_4$ rosettes-like hierarchical spinel as bifunctional materials for oxygen evolution (OER) and reduction (ORR) reactions in alkaline media. *J. Electroanal. Chem.* **2019**, *847*, 113190, https://doi.org/10.1016/j.jelechem.2019.113190.
47. Lankauf, K.; Cysewska, K.; Karczewski, J.; Mielewczyk-Gryń, A.; Górnicka, K.; Cempura, G.; Chen, M.; Jasiński, P.; Molin, S. $Mn_xCo_{3-x}O_4$ spinel oxides as efficient oxygen evolution reaction catalysts in alkaline media. *Int. J. Hydrogen Energy* **2020**, *45*, 14867–14879, https://doi.org/10.1016/j.ijhydene.2020.03.188.
48. Malaie, K.; Ganjali, M.R. Tuning CoFe and NiFe spinel oxide compositions by a fast glycine-nitrate autocombustion for oxygen evolution electrocatalysts and implications from their cyclic voltammograms on the role of Fe. *Mater. Chem. Phys.* **2020**, *253*, 123339, https://doi.org/10.1016/j.matchemphys.2020.123339.
49. Fei, B.; Chen, Z.; Ha, Y.; Wang, R.; Yang, H.; Xu, H.; Wu, R. Anion-cation co-substitution activation of spinel $CoMoO_4$ for efficient oxygen evolution reaction. *Chem. Eng. J.* **2020**, *394*, 124926, https://doi.org/10.1016/j.cej.2020.124926.
50. Bockris, J.O.; Otagawa, T. Mechanism of oxygen evolution on perovskites. *J. Phys. Chem.* **1983**, *87*, 2960–2971, https://doi.org/10.1021/j100238a048.
51. Singh, J.P.; Singh, N.K.; Singh, R.N. Electrocatalytic activity of metal—substituted Fe_3O_4 obtained at low temperature for O_2 evolution. *Int. J. Hydrogen Energy* **1999**, 24, 433–439, https://doi.org/10.1016/S03603199(98)00084-6
52. Singh, R.; Singh, J.; Lal, B.; Thomas, M.; Bera, S. New $NiFe_{2-x}Cr_xO_4$ spinel films for O_2 evolution in alkaline solutions. *Electrochimica Acta* **2006**, *51*, 5515–5523, https://doi.org/10.1016/j.electacta.2006.02.028.
53. Gaudet, J.; Tavares, A.C.; Trasatti, A.S.; Guay, D. Physicochemical Characterization of Mixed RuO_2−SnO_2 Solid Solutions. *Chem. Mater.* **2005**, *17*, 1570–1579, https://doi.org/10.1021/cm048129l.
54. Swierk, J.R.; Klaus, S.; Trotochaud, L.; Bell, A.T.; Tilley, T.D. Electrochemical Study of the Energetics of the Oxygen Evolution Reaction at Nickel Iron (Oxy)Hydroxide Catalysts. *J. Phys. Chem. C* **2015**, *119*, 19022–19029, https://doi.org/10.1021/acs.jpcc.5b05861.
55. Lyons, M.; Brandon, M.P. The significance of electrochemical impedance spectra recorded during active oxygen evolution for oxide covered Ni, Co and Fe electrodes in alkaline solution. *J. Electroanal. Chem.* **2009**, *631*, 62–70, https://doi.org/10.1016/j.jelechem.2009.03.019.
56. Vasić, M.; Cebela, M.; Pašti, I.; Amaral, L.; Hercigonja, R.; Santos, D.; Šljukić, B. Efficient hydrogen evolution electrocatalysis in alkaline medium using Pd-modified zeolite X. *Electrochimica Acta* **2018**, *259*, 882–892, https://doi.org/10.1016/j.electacta.2017.11.020.
57. Franceschini, E.A.; Lacconi, G.I.; Corti, H.R. Kinetics of the hydrogen evolution on nickel in alkaline solution: new insight from rotating disk electrode and impedance spectroscopy analysis. *Electrochimica Acta* **2015**, *159*, 210–218, https://doi.org/10.1016/j.electacta.2015.01.110.
58. Chen, Y.-Y.; Zhang, Y.; Jiang, W.-J.; Zhang, X.; Dai, Z.; Wan, L.-J.; Hu, J.-S. Pomegranate-like N,P-Doped Mo_2C@C Nanospheres as Highly Active Electrocatalysts for Alkaline Hydrogen Evolution. *ACS Nano* **2016**, *10*, 8851–8860, https://doi.org/10.1021/acsnano.6b04725.
59. Batoo, K.M. Structural and electrical properties of Cu-doped $NiFe_2O_4$ nanoparticles prepared through modified citrate gel method. *J. Phys. Chem. Solids* **2011**, *72*, 1400–1407, https://doi.org/10.1016/j.jpcs.2011.08.005.